

Supporting Information for “A nutrient effect on the TEX₈₆ paleotemperature proxy”

Ronnakrit Rattanasriampaipong^{1,2}, Jessica Tierney², Jordan T. Abell³,

Lauren D. Gilmore⁴

¹University Corporation for Atmospheric Research, Boulder, CO 80307

²Department of Geosciences, The University of Arizona, Tucson, AZ 85721

³Department of Earth and Environmental Sciences, Lehigh University, Bethlehem, PA 18015

⁴Department of Geosciences, Princeton University, Princeton, NJ 08544

Contents of this file

1. Text S1 to S3
2. Figures S1 to S9
3. Tables S1 to S3

Additional Supporting Information (Files uploaded separately)

1. Captions for Datasets S1 to S7
2. Captions for Codes S1 to S2

Corresponding author: R. Rattanasriampaipong, Department of Geosciences, University of Arizona, Gould-Simpson Building, Room 513A, Tucson, AZ 85721, USA. (rrattan@ucar.edu)

Introduction

This document provides supplementary information for the main text, including (a) supplementary texts for extended methods and materials, (b) brief descriptions of supplementary datasets and codes reposed on Zenodo (Rattanasriampaipong et al., 2025) and Github repositories (<https://github.com/PaleoLipidRR/nutrient-effect-on-TEX>), (c) supplementary figures, and (d) supplementary tables.

Text S1: Marine core-top sediments

In order to expand the TEX₈₆ coretop database, we analyzed 170 new core top samples from sediment cores stored at the Woods Hole Oceanographic Institution Seafloor Samples Repository. Whenever possible we sampled 1-2 cm from the very top of the cores (e.g., 0–1 or 0–2 cm); in cases where upper sediments were unavailable, we drew samples from as close to the top as possible (generally within the top 10 cm). The majority of these cores (>90%) were box cores, multicores, or gravity cores; samples from these types of cores should represent recent (i.e., late Holocene) conditions. The remaining samples were piston cores, where loss of modern sediment is likely due to the coring process. In this case we targeted piston cores that had confirmed Holocene sediments from previously published work.

These coretop sediment samples are the same set used in the BAYSPLINE calibration (Tierney & Tingley, 2018) and in that study, we found that their U₃₇^{K'} values overlapped well with previously analyzed data from the global dataset, suggesting they are representative of near-modern oceanographic conditions.

Text S2: Core locations, age models, and sampling for DSDP Site 591 and IODP Site U1510

Deep Sea Drilling Program (DSDP) Site 591 (31.58°S , 164.43°E , 2131 m water depth) was taken from a spur of the central Lord Howe Rise in the north Tasman Sea, just to the north of the modern Tasman Front (Kennett & Borch, 1986; Tilburg et al., 2001). International Ocean Discovery Program (IODP) Site U1510 (36.33°S , 164.56°E , 1238 m water depth) is from the southern section of the Lord Howe Rise, but south of the Tasman Front (Sutherland et al., 2019). The late Quaternary sediments in both cores are dominated by calcium carbonate (in the form of foraminifera-bearing nannofossil oozes, with trace amounts of biogenic silica and terrigenous material present (Kennett & Borch, 1986; Sutherland et al., 2019).

The sampling strategy for both cores was designed to obtain \sim 2–3-kyr resolution over the last \sim 25 kyr and across the marine isotope stage (MIS) 5–6 transition, while also maintaining \sim 5-kyr resolution for the rest of the interval back to \sim 150 ka. The initial age model for DSDP 591 was based on comparing abundances of specific planktic foraminifera (Martínez, 1994, 1997) to oxygen isotopes measured on the planktic foraminifera *Globigerina bulloides* from DSDP 591A(C. S. Nelson et al., 1993; C. Nelson et al., 1994). For IODP U1510, because no Quaternary high-resolution age model exists (the first biostratigraphic tie-point is at \sim 440 ka (Sutherland et al., 2019), we used color reflectance data from the splice and compared these to the LR04 benthic oxygen isotope stack (see Figure S9; Lisiecki & Raymo, 2005). Cycles are clearly present in the color reflectance data (Figure S9), and the calculated linear sedimentation rates (LSRs) are consistent with those produced using the lower-resolution biostratigraphy (Sutherland et al., 2019), providing confidence in our method. The ages of determined MIS boundaries for both cores were

updated to those provided by Lisiecki and Raymo (2005). Finally, we further updated the preliminary age models of DSDP 591 and IODP U1510 using additional tie-points by comparing the core-specific SSTs to the benthic oxygen isotope stack (Tables S2–3 and Figure S9).

Text S3: GDGT and alkenone determinations

Sediment samples were freeze-dried and homogenized, then ca. 5–30 grams of material were extracted using an Accelerated Solvent Extraction 350 system ($T = 100^{\circ}\text{C}$, max pressure = 1500 psi). For the core top samples, resulting total lipid extracts were run through a sodium sulfate column to remove any interstitial water, then separated into neutral, acid, and polar fractions over LC-NH₂ gel with dichloromethane(DCM):isopropanol (2:1), 4% acetic acid in DCM, and methanol as the respective eluents. The neutral and polar fractions were recombined and then separated over 5% deactivated silica gel into apolar, ketone, and polar fractions using hexane, DCM, and methanol (containing the GDGTs) as respective eluents. For the Tasman Sea sediments, a 25 ng μL^{-1} stearyl stearate standard and a 10 ng μL^{-1} C₄₆ GDGT standard were added to the total lipid extracts post-extraction. Samples were then loaded onto a column filled with a layer of LC-NH₂ gel and another layer of 5% deactivated silica. The total lipid extracts were separated in five fractions via elution with hexane, DCM, 2:1 (vol./vol.) mixture of DCM:isopropanol, 4% acetic acid in DCM, and methanol. For the purposes of this study, the DCM fraction was used for the alkenones while the 2:1 (vol./vol.) mixture of DCM:isopropanol was used for the GDGTs. The fraction containing the GDGTs in all samples was redissolved in hexane:isopropanol (99:1) then filtered through a 0.45 PTFE filter prior to analysis.

GDGTs were analyzed on an Agilent 1260 Infinity HPLC coupled to an Agilent 6120 single quadrupole mass spectrometer using two BEH HILIC silica columns (2.1 x 150 mm, 1.7 μ m, Waters) and the methodology of Hopmans et al. (2016). We integrated peak areas using the MATLAB package ORIGAmI (Fleming and Tierney, 2016). Quantification of GDGTs was achieved by comparison of the GDGTs areas to the area of the C₄₆ internal standard.

Alkenones were analyzed on a Trace 1310 gas chromatograph equipped with a DB-1 column (60 m \times 0.32 mm \times 0.1 μ m) and a programmable temperature vaporization (PTV) injector. The PTV was operated in ramped pressure mode, with injection at 14.5 psi and 60°C, held for 0.1 minute, followed by transfer at 33.6 psi and a temperature increase of 5°C/sec to 325°C, held for 3 minutes. The oven program was 60°C held for two minutes, followed by a ramp of 30°C/min to 270°C, then a ramp of 1°C/minute to 310°C, held for 1 minute, and finally a ramp of 10°C/min to 325 °C, held for 18.5 minutes. Carrier gas was helium, at a flow rate of 1.5 mL/min. Quantification of alkenones was achieved by comparison of alkenone peak areas to the peak area of the stearyl stearate internal standard.

Data Set S1.

An updated global core-top TEX₈₆ data from previous compilation efforts, including Kim, Schouten, Hopmans, Donner, and Sinninghe Damsté (2008), Kim et al. (2010), Tierney and Tingley (2014, 2015), Rattanasriampaipong, Zhang, Pearson, Hedlund, and Zhang (2022), Hagemann et al. (2023), and Varma, Hopmans, van Kemenade, et al. (2024). The dataset contains 2104 entries of isoprenoid GDGT fractional abundances from unique core-top sites, along with latitude-longitude coordinates, modern water depth (meters below sea level), calculated TEX₈₆ and BIT index values, and references/DOI for data sources.

Filename: *ds01_updated_global_coretop_tex.csv*

Data Set S2. The spreadsheet containing "regionName" labels for all coretop locations.

Filename: *ds02_manual_regionName_assigments.xlsx*

Data Set S3. A post-processed panda dataframe saved into csv file format. The updated coretop TEX₈₆ dataset (Dataset S1) with matched sea water properties, calculated GDGT-based indices, and matched "regionName" labels.

Filename: *ds03_processed_coretop_tex.csv*

Data Set S4. This dataset contains statistics of gridded coretop TEX₈₆ data. The dataset includes the median, mean, standard deviation, and count of TEX₈₆ values for each grid cell with the same lat-lon dimensions as the WOA23 temperature data (0.25° × 0.25° grid). The dataset also includes the residuals of TEX₈₆ values from the linear regression between TEX₈₆ and the surface-to-thermocline average temperature (t_sf2tc_avg) values. Coretop TEX₈₆ data included in this dataset are quality-controlled by applying

the thresholds of BIT < 0.5, MI < 0.5, and %GDGT-0 < 60%.

Filename: *ds04_gridded_coretex.nc*

Data Set S5. This dataset provides gridded ammonia oxidation data derived from the Global Nitrification Database (Tang et al., 2023). It includes statistics (count, median, mean, and standard deviation) of ammonia oxidation rates, as well as ammonium, nitrite, and nitrate concentrations, at each grid cell. The dataset is gridded at $0.25^\circ \times 0.25^\circ$ spatial resolution for consistency with WOA23 data.

Filename: *ds05_gridded_AOM.ds.nc*

Data Set S6. This dataset contains climatological annual means (1993–2022) derived from monthly climatologies of ocean properties. The variables included are:

- **no2_sf2tc_avg:** surface-to-thermocline average nitrite concentration
- **no2_tc:** nitrite concentration at the thermocline
- **t_sf2tc_avg:** surface-to-thermocline average sea water temperature
- **t_tc:** sea water temperature at the thermocline
- **tc_depth:** thermocline depth

Filename: *ds06_calculated_ocean_properties.nc*

Data Set S7. This dataset provides gridded ammonia oxidation data derived from the Global Nitrification Database (Tang et al., 2023). It includes statistics (count, median, mean, and standard deviation) of ammonia oxidation rates, as well as ammonium, nitrite, and nitrate concentrations, at each grid cell. The dataset is gridded at $0.25^\circ \times 0.25^\circ$ spatial resolution for consistency with WOA23 data.

Filename: *ds07_gridded_AOM.ds.nc*

References

- Bale, N. J., Villanueva, L., Hopmans, E. C., Schouten, S., & Sinninghe Damsté, J. S. (2013). Different seasonality of pelagic and benthic Thaumarchaeota in the North Sea. *Biogeosciences*, 10(11), 7195–7206. Retrieved from <https://bg.copernicus.org/articles/10/7195/2013/> doi: 10.5194/bg-10-7195-2013
- Castañeda, I. S., Schefuß, E., Pätzold, J., Sinnenhe Damsté, J. S., Weldeab, S., & Schouten, S. (2010, mar). Millennial-scale sea surface temperature changes in the eastern Mediterranean (Nile River Delta region) over the last 27,000 years. *Paleoceanography*, 25(1). Retrieved from <https://doi.org/10.1029/2009PA001740> doi: <https://doi.org/10.1029/2009PA001740>
- Ceccopieri, M., Carreira, R. S., Wagener, A. L. R., Hefta, J. H., & Mollenhauer, G. (2018). On the application of alkenone- and GDGT-based temperature proxies in the south-eastern Brazilian continental margin. *Organic Geochemistry*, 126, 43–56. doi: 10.1016/j.orggeochem.2018.10.009
- Chazen, C. R. (2011). *Holocene climate evolution of the eastern tropical Pacific told from high resolution climate records from the Peru margin and equatorial upwelling regions* (Doctoral dissertation, Brown University). doi: <https://doi.org/10.7301/Z0D50K7P>
- Chen, J., Hu, P., Li, X., Yang, Y., Song, J., Li, X., ... Lü, X. (2018). Impact of water depth on the distribution of iGDGTs in the surface sediments from the northern South China Sea: applicability of TEX86 in marginal seas. *Frontiers of Earth Science*, 12(1), 95–107. doi: 10.1007/s11707-016-0620-1
- Chen, W., Mohtadi, M., Schefuß, E., & Mollenhauer, G. (2014). Organic-geochemical proxies of sea surface temperature in surface sediments of the tropical eastern Indian Ocean. *Deep Sea Research Part I: Oceanographic Research Papers*, 88, 17–29. doi:

<https://doi.org/10.1016/j.dsr.2014.03.005>

- Fallet, U., Castañeda, I. S., Henry-Edwards, A., Richter, T. O., Boer, W., Schouten, S., & Brummer, G.-J. (2012, jan). Sedimentation and burial of organic and inorganic temperature proxies in the Mozambique Channel, SW Indian Ocean. *Deep Sea Research Part I: Oceanographic Research Papers*, 59, 37–53. doi: 10.1016/j.dsr.2011.10.002
- Hagemann, J. R., Lembke-Jene, L., Lamy, F., Vorrath, M.-E., Kaiser, J., Müller, J., ... Tiedemann, R. (2023). *Collection of GDGT-derived temperatures of 22 new sites at the Chilean margin, supplemented by various previously published sites*. [Dataset]. PANGAEA. doi: 10.1594/PANGAEA.964270
- Harning, D. J., Andrews, J. T., Belt, S. T., Cabedo-Sanz, P., Geirdottir, A., Dildar, N., ... Sepúlveda, J. (2019). Sea Ice Control on Winter Subsurface Temperatures of the North Iceland Shelf During the Little Ice Age: A TEX86 Calibration Case Study. *Paleoceanography and Paleoclimatology*, 34(6), 1006–1021. doi: 10.1029/2018PA003523
- Harning, D. J., Holman, B., Woelders, L., Jennings, A. E., & Sepúlveda, J. (2023). Biomarker characterization of the North Water Polynya, Baffin Bay: implications for local sea ice and temperature proxies. *Biogeosciences*, 20(1), 229–249. Retrieved from <https://doi.org/10.1594/PANGAEA.956212> <https://bg.copernicus.org/articles/20/229/2023/> doi: 10.5194/bg-20-229-2023
- Hernández-Sánchez, M. T., Woodward, E. M. S., Taylor, K. W. R., Henderson, G. M., & Pancost, R. D. (2014). Variations in GDGT distributions through the water column in the South East Atlantic Ocean. *Geochimica et Cosmochimica Acta*, 132, 337–348. doi: <https://doi.org/10.1016/j.gca.2014.02.009>
- Ho, S. L., Mollenhauer, G., Fietz, S., Martínez-Garcia, A., Lamy, F., Rueda, G., ...

- Tiedemann, R. (2014). Appraisal of TEX86 and TEX86L thermometries in subpolar and polar regions. *Geochimica et Cosmochimica Acta*, 131, 213–226. doi: <https://doi.org/10.1016/j.gca.2014.01.001>
- Ho, S. L., Yamamoto, M., Mollenhauer, G., & Minagawa, M. (2011). Core top TEX86 values in the south and equatorial Pacific. *Organic Geochemistry*, 42(1), 94–99. doi: <https://doi.org/10.1016/j.orggeochem.2010.10.012>
- Hu, J., Meyers, P. A., Chen, G., Peng, P., & Yang, Q. (2012). Archaeal and bacterial glycerol dialkyl glycerol tetraethers in sediments from the Eastern Lau Spreading Center, South Pacific Ocean. *Organic Geochemistry*, 43, 162–167. doi: <https://doi.org/10.1016/j.orggeochem.2011.10.012>
- Jaeschke, A., Wengler, M., Hefter, J., Ronge, T. A., Geibert, W., Mollenhauer, G., ... Lamy, F. (2017). A biomarker perspective on dust, productivity, and sea surface temperature in the Pacific sector of the Southern Ocean. *Geochimica et Cosmochimica Acta*, 204, 120–139. doi: 10.1016/j.gca.2017.01.045
- Jia, G., Zhang, J., Chen, J., Peng, P., & Zhang, C. L. (2012). Archaeal tetraether lipids record subsurface water temperature in the South China Sea. *Organic Geochemistry*, 50, 68–77. doi: <https://doi.org/10.1016/j.orggeochem.2012.07.002>
- Kaiser, J., Ruggieri, N., Hefter, J., Siegel, H., Mollenhauer, G., Arz, H. W., & Lamy, F. (2014). Lipid biomarkers in surface sediments from the Gulf of Genoa, Ligurian sea (NW Mediterranean sea) and their potential for the reconstruction of palaeo-environments. *Deep Sea Research Part I: Oceanographic Research Papers*, 89, 68–83. Retrieved from <https://www.sciencedirect.com/science/article/pii/S0967063714000661> doi: <https://doi.org/10.1016/j.dsr.2014.04.009>
- Kaiser, J., Schouten, S., Kilian, R., Arz, H. W., Lamy, F., & Sinninghe Damsté, J. S.

(2015). Isoprenoid and branched GDGT-based proxies for surface sediments from marine, fjord and lake environments in Chile. *Organic Geochemistry*, 89-90, 117–127. doi: 10.1016/j.orggeochem.2015.10.007

Kennett, J. P., & Borch, C. (1986). Initial reports of the deep sea drilling project, 90..

Retrieved from <https://api.semanticscholar.org/CorpusID:132141153>

Kim, J.-H., Schouten, S., Hopmans, E. C., Donner, B., & Sinninghe Damsté, J. S. (2008).

Global sediment core-top calibration of the TEX86 paleothermometer in the ocean. *Geochimica et Cosmochimica Acta*, 72(4), 1154–1173. doi: <https://doi.org/10.1016/j.gca.2007.12.010>

Kim, J.-H., Schouten, S., Rodrigo-Gámiz, M., Rampen, S., Marino, G., Huguet, C., ...

Sinninghe Damsté, J. S. (2015). Influence of deep-water derived isoprenoid tetraether lipids on the TEX86H paleothermometer in the Mediterranean Sea. *Geochimica et Cosmochimica Acta*, 150, 125–141. doi: 10.1016/j.gca.2014.11.017

Kim, J.-H., van der Meer, J., Schouten, S., Helmke, P., Willmott, V., Sangiorgi, F., ... Sinnenhe Damsté, J. S. (2010). New indices and calibrations derived from the distribution of crenarchaeal isoprenoid tetraether lipids: Implications for past sea surface temperature reconstructions. *Geochimica et Cosmochimica Acta*, 74(16), 4639–4654. doi: 10.1016/j.gca.2010.05.027

Kim, J.-H., Villanueva, L., Zell, C., & Sinnenhe Damsté, J. S. (2016). Biological source and provenance of deep-water derived isoprenoid tetraether lipids along the Portuguese continental margin. *Geochimica et Cosmochimica Acta*, 172, 177–204. doi: 10.1016/j.gca.2015.09.010

Kusch, S., Rethemeyer, J., Hopmans, E. C., Wacker, L., & Mollenhauer, G. (2016). Factors influencing 14C concentrations of algal and archaeal lipids and their associated

sea surface temperature proxies in the Black Sea. *Geochimica et Cosmochimica Acta*, 188, 35–57. doi: 10.1016/j.gca.2016.05.025

Lamping, N., Müller, J., Hefter, J., Mollenhauer, G., Haas, C., Shi, X., ... Hillenbrand, C.-D. (2021). Evaluation of lipid biomarkers as proxies for sea ice and ocean temperatures along the Antarctic continental margin. *Climate of the Past*, 17(5), 2305–2326. doi: 10.5194/cp-17-2305-2021

Leider, A., Hinrichs, K.-U., Mollenhauer, G., & Versteegh, G. J. M. (2010). Core-top calibration of the lipid-based U37K' and TEX86 temperature proxies on the southern Italian shelf (SW Adriatic Sea, Gulf of Taranto). *Earth and Planetary Science Letters*, 300(1), 112–124. doi: <https://doi.org/10.1016/j.epsl.2010.09.042>

Lengger, S. K., Hopmans, E. C., Sinninghe Damsté, J. S., & Schouten, S. (2014). Fossilization and degradation of archaeal intact polar tetraether lipids in deeply buried marine sediments (Peru Margin). *Geobiology*, 12(3), 212–220. doi: <https://doi.org/10.1111/gbi.12081>

Lisiecki, L. E., & Raymo, M. E. (2005). A Pliocene-Pleistocene stack of 57 globally distributed benthic $\delta^{18}\text{O}$ records. *Paleoceanography*, 20(1). doi: 10.1029/2004pa001071

Liu, X.-L., Zhu, C., Wakeham, S. G., & Hinrichs, K.-U. (2014). In situ production of branched glycerol dialkyl glycerol tetraethers in anoxic marine water columns. *Marine Chemistry*, 166, 1–8. Retrieved from <https://www.sciencedirect.com/science/article/pii/S0304420314001388> doi: <https://doi.org/10.1016/j.marchem.2014.08.008>

Lo, L., Belt, S. T., Lattaud, J., Friedrich, T., Zeeden, C., Schouten, S., ... Hodell, D. A. (2018). Precession and atmospheric CO₂ modulated variability of sea ice in the

- central Okhotsk Sea since 130,000 years ago. *Earth and Planetary Science Letters*, 488, 36–45. doi: 10.1016/j.epsl.2018.02.005
- Lü, X., Yang, H., Song, J., Versteegh, G. J. M., Li, X., Yuan, H., ... Xie, S. (2014). Sources and distribution of isoprenoid glycerol dialkyl glycerol tetraethers (GDGTs) in sediments from the east coastal sea of China: Application of GDGT-based paleothermometry to a shallow marginal sea. *Organic Geochemistry*, 75, 24–35. doi: <https://doi.org/10.1016/j.orggeochem.2014.06.007>
- Martínez, J. (1994). Late Pleistocene palaeocenography of the Tasman Sea: Implications for the dynamics of the warm pool in the western Pacific. *Palaeogeography, Palaeoclimatology, Palaeoecology*, 112(1), 19–62. Retrieved from <https://www.sciencedirect.com/science/article/pii/0031018294901333> doi: [https://doi.org/10.1016/0031-0182\(94\)90133-3](https://doi.org/10.1016/0031-0182(94)90133-3)
- Martínez, J. (1997). Decreasing influence of subantarctic mode water north of the tasman front over the past 150 kyr. *Palaeogeography, Palaeoclimatology, Palaeoecology*, 131, 355–364. doi: [https://doi.org/10.1016/S0031-0182\(97\)00011-4](https://doi.org/10.1016/S0031-0182(97)00011-4)
- Nelson, C., Hendy, C., & Cuthbertson, A. (1994). Oxygen isotope evidence for climatic contrasts between tasman sea and southwest pacific ocean during the late quaternary. In *Tasman sea conference* (pp. 181–196).
- Nelson, C. S., Hendy, C. H., & Cuthbertson, A. M. (1993). *Compendium of stable oxygen and carbon isotope data for the late quaternary interval of deep-sea cores from the new zealand sector of the tasman sea and southwest pacific ocean*. Department of Earth Sciences, University of Waikato.
- Nieto-Moreno, V., Martínez-Ruiz, F., Willmott, V., García-Orellana, J., Masqué, P., & Sinninghe Damsté, J. S. (2013). Climate conditions in the westernmost Mediter-

- ranean over the last two millennia: An integrated biomarker approach. *Organic Geochemistry*, 55, 1–10. doi: <https://doi.org/10.1016/j.orggeochem.2012.11.001>
- Pan, A., Yang, Q., Zhou, H., Ji, F., Wang, H., & Pancost, R. D. (2016). A diagnostic GDGT signature for the impact of hydrothermal activity on surface deposits at the Southwest Indian Ridge. *Organic Geochemistry*, 99, 90–101.
- Park, Y.-H., Yamamoto, M., Nam, S.-I., Irino, T., Polyak, L., Harada, N., ... Saitoh, S.-I. (2014). Distribution, source and transportation of glycerol dialkyl glycerol tetraethers in surface sediments from the western Arctic Ocean and the northern Bering Sea. *Marine Chemistry*, 165, 10–24. doi: <https://doi.org/10.1016/j.marchem.2014.07.001>
- Rattanasriampaipong, R., Tierney, J., & Abell, J. (2025). *Supplementary Data for ‘A nutrient effect on the TEX₈₆ paleotemperature proxy’*. [Dataset]. Zenodo. doi: 10.5281/zenodo.14806962
- Rattanasriampaipong, R., Zhang, Y. G., Pearson, A., Hedlund, B. P., & Zhang, S. (2022). Archaeal lipids trace ecology and evolution of marine ammonia-oxidizing archaea. *Proceedings of the National Academy of Sciences*, 119(31), e2123193119. doi: 10.1073/pnas.2123193119
- Richey, J. N., Hollander, D. J., Flower, B. P., & Eglington, T. I. (2011, mar). Merging late Holocene molecular organic and foraminiferal-based geochemical records of sea surface temperature in the Gulf of Mexico. *Paleoceanography*, 26(1). doi: <https://doi.org/10.1029/2010PA002000>
- Richey, J. N., & Tierney, J. E. (2016). GDGT and alkenone flux in the northern Gulf of Mexico: Implications for the TEX86 and UK₃₇' paleothermometers. *Paleoceanography*, 31(12), 1547–1561. doi: 10.1002/2016pa003032

- Rodrigo-Gámiz, M., Rampen, S. W., de Haas, H., Baas, M., Schouten, S., & Sinninghe Damsté, J. S. (2015). Constraints on the applicability of the organic temperature proxies UK₃₇', TEX₈₆ and LDI in the subpolar region around Iceland. *Biogeosciences*, 12(22), 6573–6590. doi: 10.5194/bg-12-6573-2015
- Schukies, J. (2018). *Concentrations of glycerol dialkyl glycerol tetraethers (GDGTs) in core top sediments from continental slope off Newfoundland, Orphan Knoll Region.* [Dataset]. PANGAEA. doi: 10.1594/PANGAEA.894305
- Seki, O., Bendle, J. A., Harada, N., Kobayashi, M., Sawada, K., Moossern, H., ... Sakamoto, T. (2014). Assessment and calibration of TEX86 paleothermometry in the Sea of Okhotsk and sub-polar North Pacific region: Implications for paleoceanography. *Progress in Oceanography*, 126, 254–266. doi: <https://doi.org/10.1016/j.pocean.2014.04.013>
- Seki, O., Sakamoto, T., Sakai, S., Schouten, S., Hopmans, E. C., Sinnenhe Damste, J. S., & Pancost, R. D. (2009). Large changes in seasonal sea ice distribution and productivity in the Sea of Okhotsk during the deglaciations. *Geochemistry, Geophysics, Geosystems*, 10(10). doi: <https://doi.org/10.1029/2009GC002613>
- Shevenell, A. E., Ingalls, A. E., Domack, E. W., & Kelly, C. (2011). Holocene Southern Ocean surface temperature variability west of the Antarctic Peninsula. *Nature*, 470(7333), 250–254. doi: 10.1038/nature09751
- Sinninghe Damsté, J. S. (2016). Spatial heterogeneity of sources of branched tetraethers in shelf systems: The geochemistry of tetraethers in the Berau River delta (Kalimantan, Indonesia). *Geochimica et Cosmochimica Acta*, 186, 13–31. doi: 10.1016/j.gca.2016.04.033
- Sinninghe Damsté, J. S., Warden, L. A., Berg, C., Jürgens, K., & Moros, M. (2022). Eval-

uation of the distributions of hydroxylated glycerol dibiphytanyl glycerol tetraethers (GDGTs) in Holocene Baltic Sea sediments for reconstruction of sea surface temperature: the effect of changing salinity. *Climate of the Past*, 18(10), 2271–2288. doi: 10.5194/cp-18-2271-2022

Smith, M., De Deckker, P., Rogers, J., Brocks, J., Hope, J., Schmidt, S., ... Schouten, S. (2013). Comparison of U37K', TEX86H and LDI temperature proxies for reconstruction of south-east Australian ocean temperatures. *Organic Geochemistry*, 64, 94–104. doi: <https://doi.org/10.1016/j.orggeochem.2013.08.015>

Sutherland, R., Dickens, G. R., Blum, P., & the Expedition 317 Scientists. (2019). Tasman Frontier Subduction Initiation and Paleogene Climate. *Proceedings of the International Ocean Discovery Program*, 371, 1–44.

Tang, W., Ward, B. B., Beman, M., Bristow, L., Clark, D., Fawcett, S., ... Zhang, Y. (2023). Database of nitrification and nitrifiers in the global ocean. *Earth System Science Data*, 15(11), 5039–5077. doi: 10.5194/essd-15-5039-2023

Tierney, J. E., & Tingley, M. P. (2014). A Bayesian, spatially-varying calibration model for the TEX86 proxy. *Geochimica et Cosmochimica Acta*, 127, 83–106. doi: 10.1016/j.gca.2013.11.026

Tierney, J. E., & Tingley, M. P. (2015). A TEX 86 surface sediment database and extended Bayesian calibration. *Scientific Data*, 2(1), 1–10.

Tierney, J. E., & Tingley, M. P. (2018). BAYSPLINE: A New Calibration for the Alkenone Paleothermometer. *Paleoceanography and Paleoclimatology*, 33(3), 281–301. doi: 10.1002/2017PA003201

Tierney, J. E., Ummenhofer, C. C., & DeMenocal, P. B. (2015). Past and future rainfall in the Horn of Africa. *Science Advances*, 1(9), e1500682. doi: 10.1126/sciadv.1500682

- Tilburg, C. E., Hurlbut, H. E., O'Brien, J. J., & Shriver, J. F. (2001). The dynamics of the east australian current system: The tasman front, the east auckland current, and the east cape current. *Journal of Physical Oceanography*, 31, 2917 - 2943. doi: 10.1175/1520-0485(2001)031<2917:TDOTEA>2.0.CO;2
- Trommer, G., Siccha, M., van der Meer, M. T. J., Schouten, S., Sinninghe Damsté, J. S., Schulz, H., ... Kucera, M. (2009). Distribution of Crenarchaeota tetraether membrane lipids in surface sediments from the Red Sea. *Organic Geochemistry*, 40(6), 724–731. doi: 10.1016/j.orggeochem.2009.03.001
- Varma, D., Hopmans, E. C., van Kemenda, Z. R., Kusch, S., Berg, S., Bale, N. J., ... Schouten, S. (2024). Evaluating isoprenoidal hydroxylated GDGT-based temperature proxies in surface sediments from the global ocean. *Geochimica et Cosmochimica Acta*, 370, 113–127. doi: 10.1016/j.gca.2023.12.019
- Varma, D., Hopmans, E. C., van Kemenda, Z. R., Kusch, S., Berg, S., Bale, N. J., ... Schouten, S. (2024). *OHGDGT global surface sediment data*. [Dataset]. PANGAEA. doi: 10.1594/PANGAEA.964885
- Verleye, T. J. (2011). *The late Quaternary palaeoenvironmental changes along the western South-American continental slope: A reconstruction based on dinoflagellate cysts and TEX86* (PhD Thesis, Ghent University). Retrieved from <https://www.vliz.be/en/imis?module=ref&refid=210274>
- Wei, B., Jia, G., Hefter, J., Kang, M., Park, E., Wang, S., & Mollenhauer, G. (2020). Comparison of the UK'37, LDI, TEX^H₈₆, and RI-OH temperature proxies in sediments from the northern shelf of the South China Sea. *Biogeosciences*, 17(17), 4489–4508. doi: 10.5194/bg-17-4489-2020
- Wei, Y., Wang, J., Liu, J., Dong, L., Li, L., Wang, H., ... Zhang, C. L. (2011). Spatial

Variations in Archaeal Lipids of Surface Water and Core-Top Sediments in the South China Sea and Their Implications for Paleoclimate Studies. *Applied and Environmental Microbiology*, 77(21), 7479–7489. doi: 10.1128/aem.00580-11

Wu, W., Tan, W., Zhou, L., Yang, H., & Xu, Y. (2012, jul). Sea surface temperature variability in southern Okinawa Trough during last 2700 years. *Geophysical Research Letters*, 39(14). doi: <https://doi.org/10.1029/2012GL052749>

Yang, Y., Gao, C., Dang, X., Ruan, X., Lü, X., Xie, S., ... Yang, H. (2018). Assessing hydroxylated isoprenoid GDGTs as a paleothermometer for the tropical South China Sea. *Organic Geochemistry*, 115, 156–165. doi: 10.1016/j.orggeochem.2017.10.014

Zell, C., Kim, J.-H., Hollander, D., Lorenzoni, L., Baker, P., Silva, C. G., ... Sininghe Damsté, J. S. (2014). Sources and distributions of branched and isoprenoid tetraether lipids on the Amazon shelf and fan: Implications for the use of GDGT-based proxies in marine sediments. *Geochimica et Cosmochimica Acta*, 139, 293–312. Retrieved from <http://www.sciencedirect.com/science/article/pii/S0016703714002968> doi: <https://doi.org/10.1016/j.gca.2014.04.038>

Zhou, H., Hu, J., Spiro, B., Peng, P., & Tang, J. (2014). Glycerol dialkyl glycerol tetraethers in surficial coastal and open marine sediments around China: Indicators of sea surface temperature and effects of their sources. *Palaeogeography, Palaeoclimatology, Palaeoecology*, 395, 114–121. Retrieved from <https://www.sciencedirect.com/science/article/pii/S0031018213005361> doi: <https://doi.org/10.1016/j.palaeo.2013.12.006>

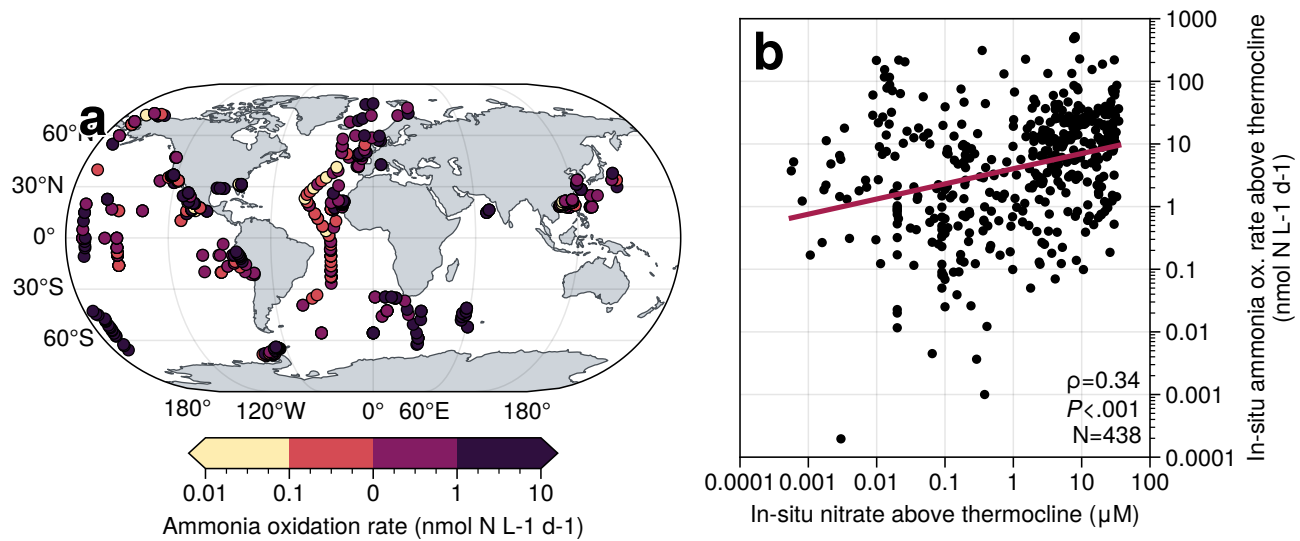


Figure S1. Ocean surface nitrate concentrations correlate with ammonia oxidation rates. (a) Spatial distribution of gridded ammonia oxidation rates above the thermocline. (b) Relationship between ammonia oxidation rates and nitrate concentrations. Measurements of ammonia oxidation rates and bioavailable nitrogen are co-located. Data were obtained from the global nitrification database (Tang et al., 2023).

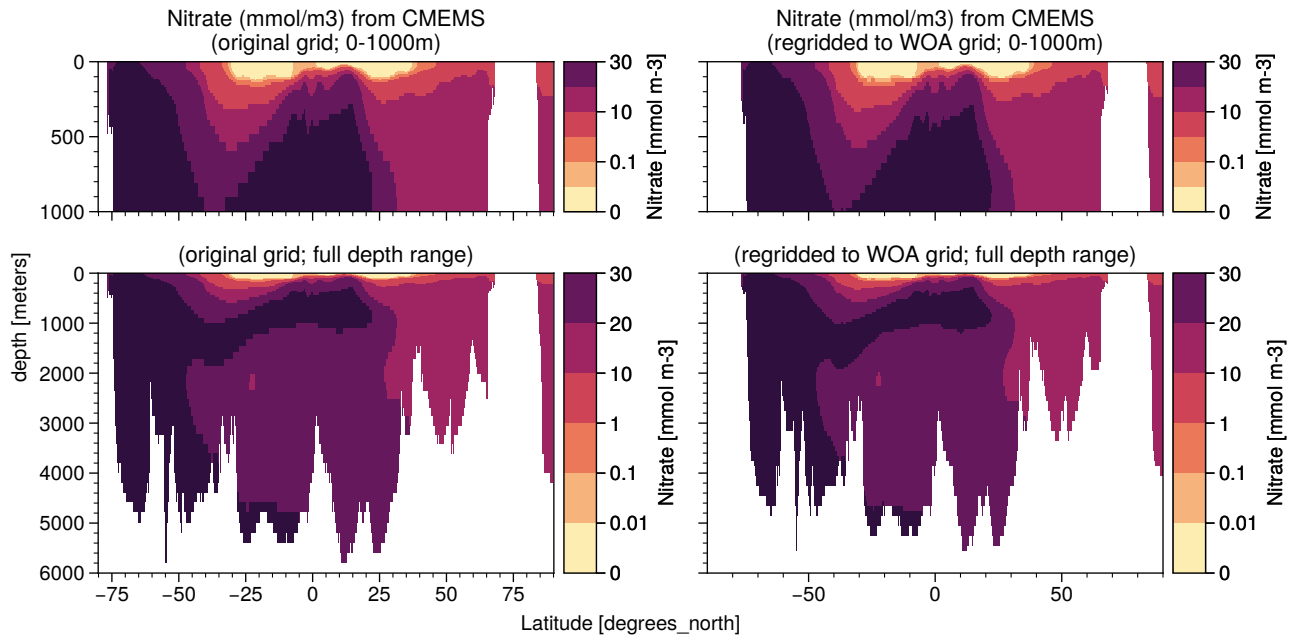


Figure S2. An example of CMEMS nitrate zonal cross section along 30° longitude.

Nitrate concentration profiles from the European Union Copernicus Marine and Environment Monitoring Service (CMEMS), showing (left) the original dataset and (right) the same dataset re-gridded to the World Ocean Atlas 2023 (WOA23) grid. The original dataset represents the 1993–2022 climatological mean field, derived from monthly data. The top row presents nitrate distributions for the upper 1000 meters of the water column, while the bottom row extends to the full depth range. The re-gridding was performed to ensure coordinate consistency with WOA23, facilitating direct comparisons with temperature and other oceanographic variables. The color scale represents nitrate concentrations in mmol m^{-3}

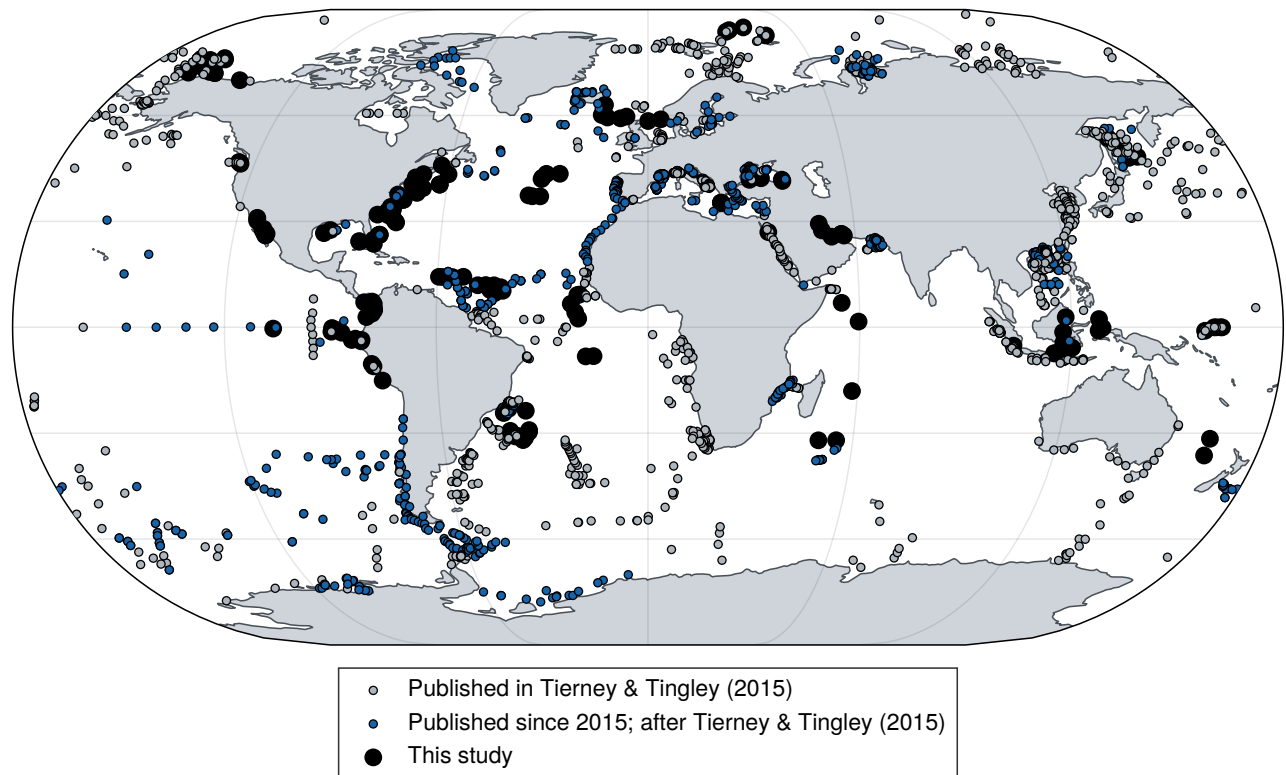


Figure S3. The distribution of an extended global core-top TEX₈₆ dataset. Data published in Tierney and Tingley (2015) are plotted in grey. Additional published datasets since 2015 are plotted in blue. New GDGT measurements from this study are plotted in black.

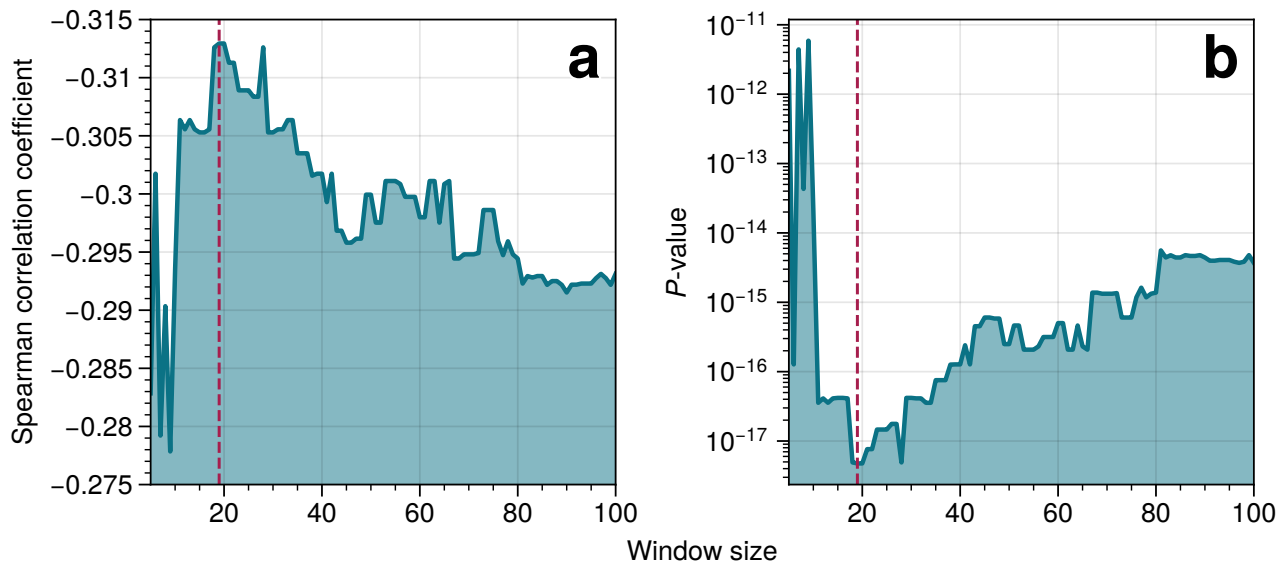


Figure S4. Sliding window analysis of Spearman correlation coefficients between thermocline-integrated nitrate concentrations and TEX₈₆ residuals as a function of window size. (a) Spearman correlation coefficient values and (b) corresponding p-values of the correlation analysis using window sizes ranging from 5 to 100 with an incremental step of 1.

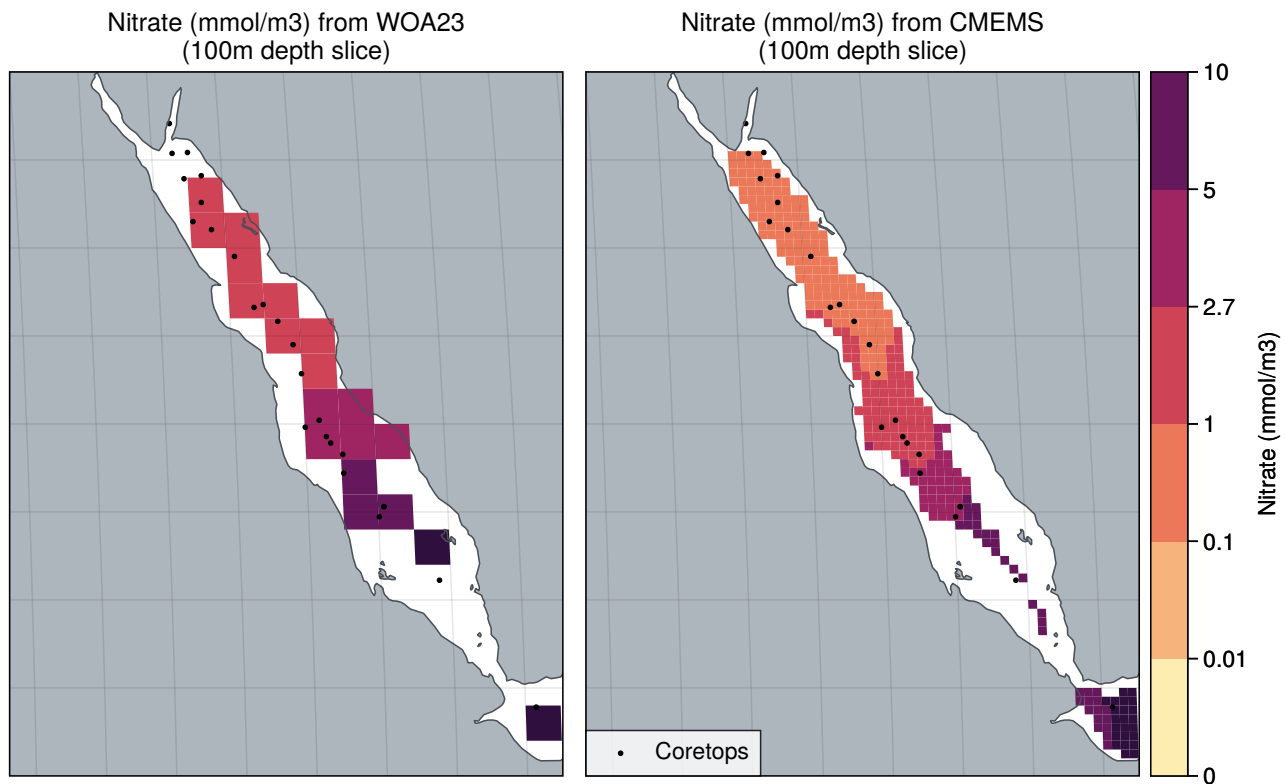


Figure S5. Comparison of nitrate concentrations at 100 m depth in the Red Sea from WOA23 and CMEMS. Maps showing nitrate concentrations (mmol/m^3) at 100 m depth from two different oceanographic datasets. (Left) Nitrate concentrations from the World Ocean Atlas 2023 (WOA23). (Right) Nitrate concentrations from the Copernicus Marine Environment Monitoring Service (CMEMS). Black dots indicate the locations of core-top sediment samples with available TEX_{86} measurements. The color scale represents nitrate concentrations on a logarithmic scale, highlighting spatial differences between the datasets.

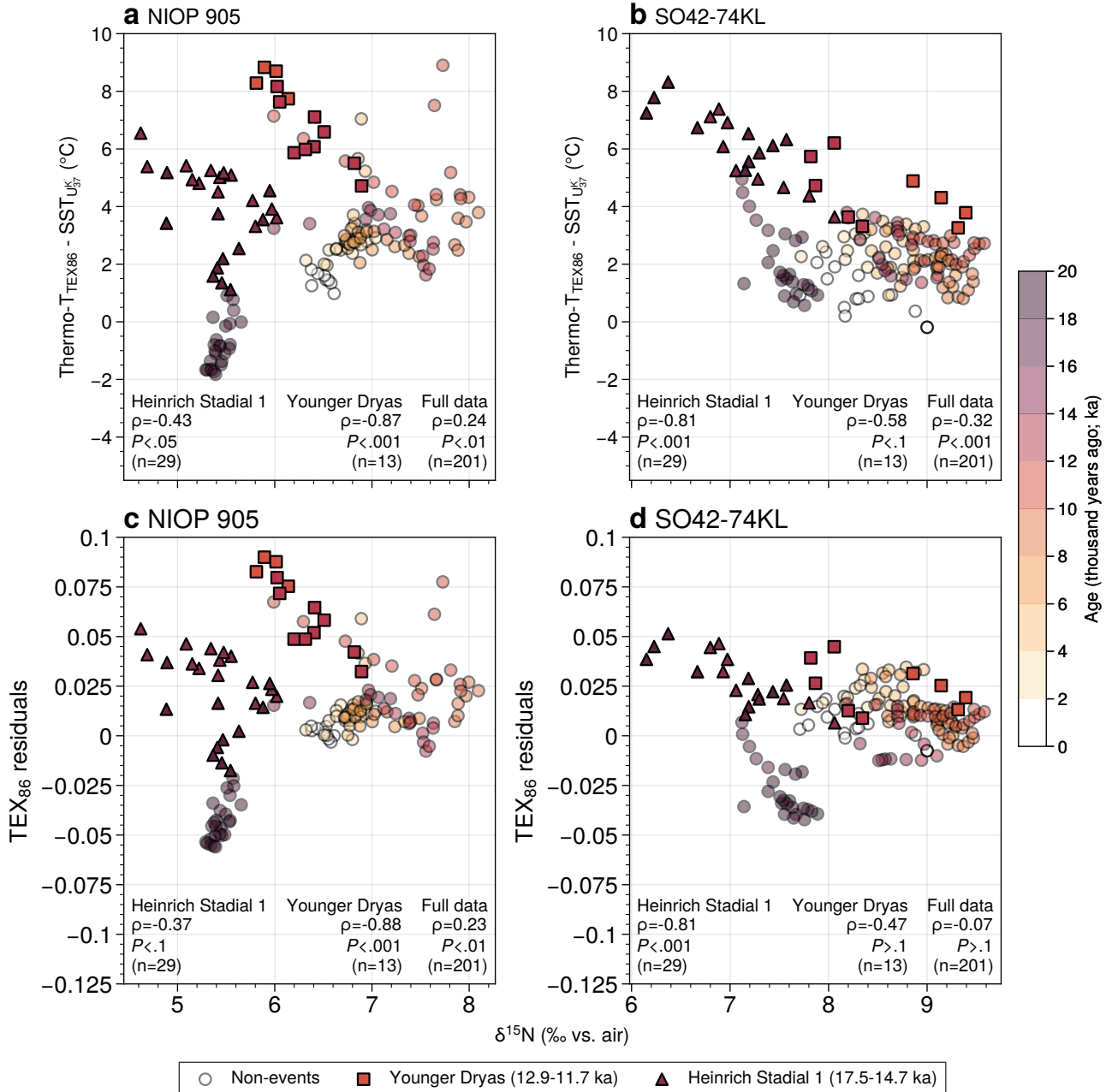


Figure S6. TEX₈₆ T anomalies correlate with bulk sediment $\delta^{15}\text{N}$. Interpolated paleo-records from core sites (left) NIOP905 and (right) SO42-74KL, with a 100-year timestep calculated from the original records shown in Figures 4B–C. (a, b) TEX₈₆ warming anomalies (Thermo-T_{TEX₈₆} - SST_{U_{37'}}) correlate negatively with bulk sediment $\delta^{15}\text{N}$, with stronger correlations observed during the Younger Dryas and Heinrich Stadial 1 events. (c, d) TEX₈₆ residuals respond to varying levels of bulk sediment $\delta^{15}\text{N}$ similarly to TEX₈₆ warming anomalies.

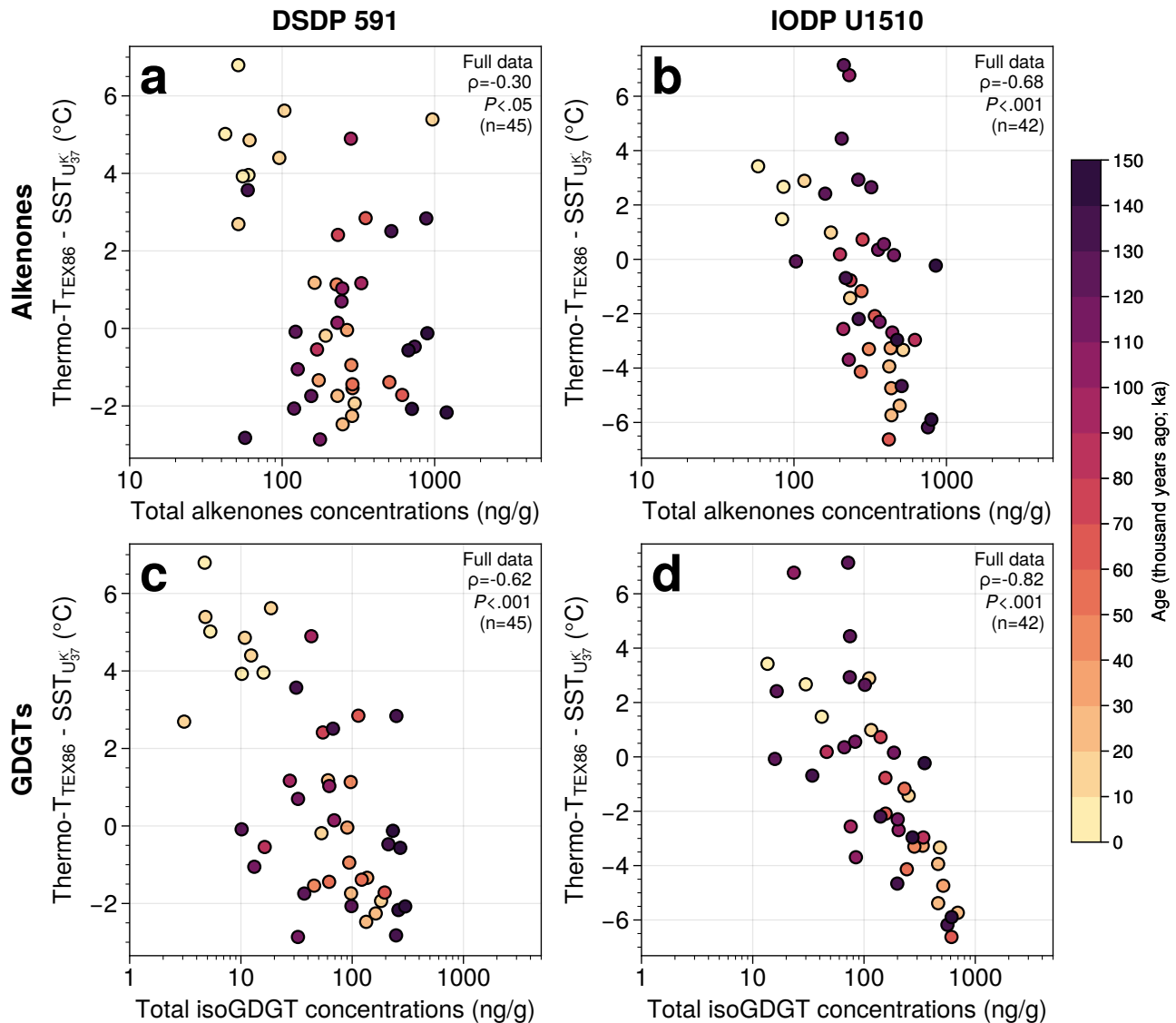


Figure S7. TEX₈₆ T anomalies correlate with bulk sediment $\delta^{15}\text{N}$. (a,b) Cross plots between alkenone concentrations and T anomalies (Thermo-T_{TEX86} - SST_{U₃₇K'}) for DSDP Site 591. (c,d) same as (a,b) but for IODP Site U1510. Data colored by sample age.

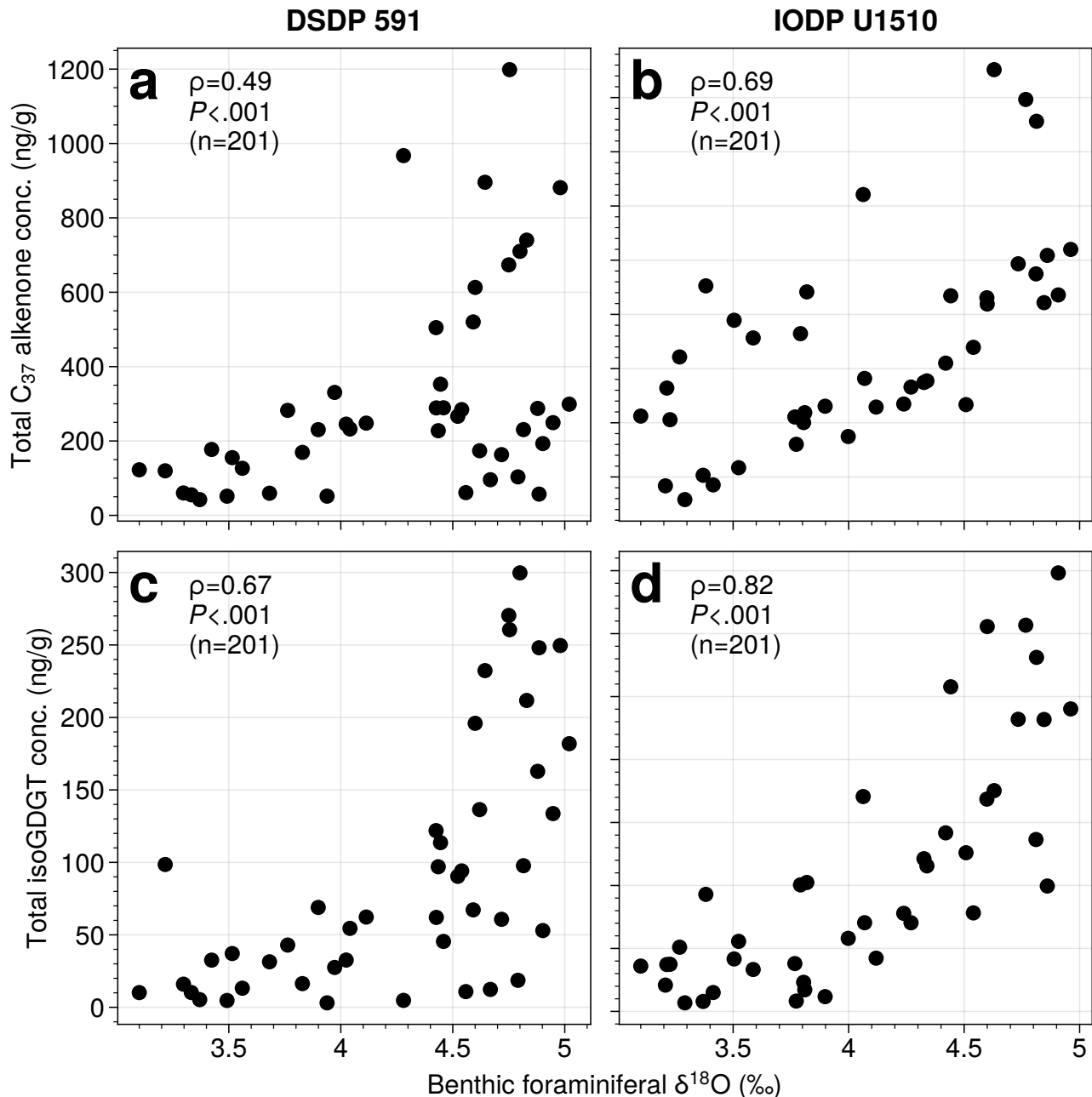


Figure S8. Biomarker concentrations correlate with benthic foraminiferal $\delta^{18}\text{O}$ stack. (a,b) Cross plots between alkenone concentrations and benthic foraminiferal $\delta^{18}\text{O}$ (Lisiecki & Raymo, 2005) interpolated to the same age step as biomarker data. (c,d) same as (a,b) but for IODP Site U1501.

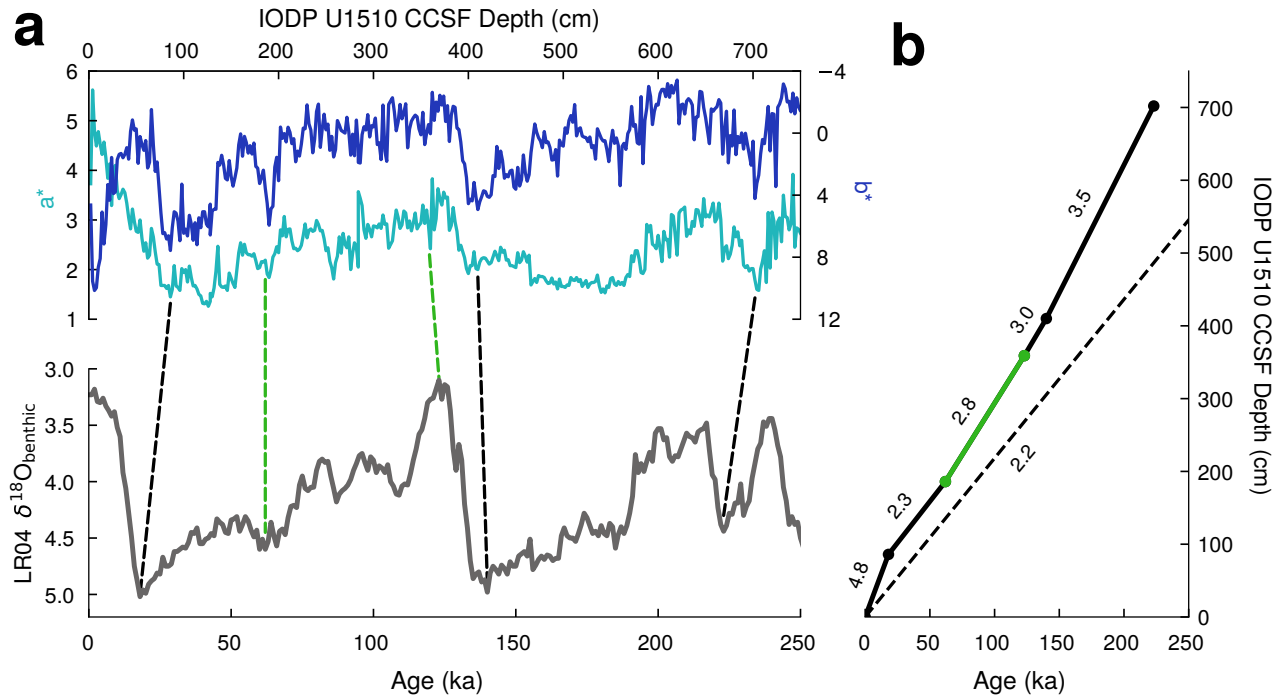


Figure S9. Construction of late Quaternary age model for IODP Site U1510. benthic foraminiferal $\delta^{18}\text{O}$ stack. (a) Core reflectance data (a^* and b^*) for IODP Site U1510 compared to the benthic foraminiferal $\delta^{18}\text{O}$ stack of Lisiecki and Raymo (2005). Black dotted lines indicate selected tie-points based on minima in b^* matched to maxima in $\delta^{18}\text{O}$. Green dotted lines denote tie-points based on Site U1510 SSTs. Specifically, the lowest SST found during MIS 4 and the highest observed during MIS 5e were matched to the respective highest and lowest $\delta^{18}\text{O}$ values during those intervals. (b) Age-depth curve for the constructed age model. Values are calculated linear sedimentation rates. The dotted line represents the age-depth curve and associated linear sedimentation rate between the core-top and the first biostratigraphic tie-point.

Table S1. Summary of coretop GDGT data sources

Remark	Reference	Count
Data from original source	Rattanasriampaipong et al. (2025) (this study) Ceccopieri et al. (2018) J. Chen et al. (2018) Hagemann et al. (2023) Harnig et al. (2019)** Harnig et al. (2023) Kusch et al. (2016) Liu et al. (2014)** Richey and Tierney (2016) Rodrigo-Gámiz et al. (2015)* Schukies (2018) Tierney and Tingley (2015) Tierney et al. (2015) Varma et al. (2024) B. Wei et al. (2020)	170 53 28 21 12 12 24 12 3 10 10 26 1 224 23
Data published in Tierney and Tingley (2014, 2015)	Castañeda et al. (2010)* Chazen (2011)* W. Chen et al. (2014) Fallet et al. (2012)*** Hernández-Sánchez (2014) Ho et al. (2011) Ho et al. (2014) Hu et al. (2012) Jia et al. (2012) Kaiser et al. (2014) Kim et al. (2008) Kim et al. (2010) Leider et al. (2010) Lengger et al. (2014) Lü et al. (2014) Nieto-Moreno et al. (2013)* Park et al. (2014) Richey et al. (2011)* Seki et al. (2009)* Seki et al. (2014) Shevenell et al. (2011)* Smith et al. (2013)* Trommer et al. (2009) Verleye (2011)* Y. Wei et al. (2011) Wu et al. (2012) Zell et al. (2014) Zhou et al. (2014)	1 4 36 10 7 20 161 7 32 29 238 158 46 10 58 2 54 1 1 58 8 14 20 1 11 1 16 27
Data retrieved from Rattanasriampaipong et al. (2022)	Kim et al. (2015) Kim et al. (2016) Pan et al. (2016)	146 31 13
Data retrieved from Hagemann et al. (2023)	Jaeschke et al. (2017) Kaiser et al. (2015) Lamping et al. (2021)	52 23 66
Data retrieved from Varma et al. (2024)	Yang et al. (2018)	23
Reanalyzed samples by Varma et al. (2024)	Bale et al. (2013) Lo et al. (2018) Sinninghe Damsté (2016) Sinninghe Damsté et al. (2022)	6 12 39 13
	Total	2084

* Only reported TEX₈₆ values are available.

** TEX₈₆ values were not available from original publications. Data were provided by corresponding authors.

*** We reported here one additional unpublished data.

DSDP 591		
Depth (mbsf)	Age* (ka)	Notes
0.00	0	†
0.30	14	†
0.49	18	‡
1.36	62	‡
2.11	123	‡
2.35	140	‡
2.95	191	†

Table S2. Age-depth model for DSDP Site 591

* Ages based on Marine Isotope Stage (MIS) maxima, minima, or transitions identified in LR04 dataset (Lisiecki & Raymo, 2005).

† Tie-point selected using planktonic foraminiferal species % (Martínez, 1994, 1997).

‡ Tie-point selected using alkenone-derived SSTs (this study).

IODP U1510		
Depth (CCSF mbsf)	Age* (ka)	Notes
0.00	0	†
0.86	18	†
1.86	62	‡
3.59	123	‡
4.10	140	†
7.02	223	†

Table S3. Age-depth model for DSDP Site 591

* Ages based on Marine Isotope Stage (MIS) maxima, minima, or transitions identified in LR04 dataset (Lisiecki & Raymo, 2005).

† Tie-point selected using color reflectance data (Sutherland et al., 2019).

‡ Tie-point selected using alkenone-derived SSTs (this study).